Structure and electronic properties of epitaxial fluorite-type $IrSi_2$ on Si(001)

Ute Hörmann,[1,*] Thilo Remmele,[1,†] John E. Klepeis,[2] Oleg Pankratov,[3] Holger Grünleitner,[4] Max Schulz,[4] Meiken Falke,[5,‡] and Andrew Bleloch[5]

[1]*Lehrstuhl für Mikrocharakterisierung, Universität Erlangen-Nürnberg, Cauerstrasse 6, 91058 Erlangen, Germany*
[2]*Lawrence Livermore National Laboratory, Livermore, California 94551, USA*
[3]*Lehrstuhl für Theoretische Festkörperphysik, Universität Erlangen-Nürnberg, Staudtstrasse 7, 91058 Erlangen, Germany*
[4]*Lehrstuhl für Angewandte Physik, Universität Erlangen-Nürnberg, Staudtstrasse 7, 91058 Erlangen, Germany*
[5]*UK SuperSTEM Laboratory, Daresbury Laboratory, Daresbury, Cheshire, WA4 4AD, United Kingdom*
(Received 16 November 2008; published 31 March 2009)

An epitaxially stabilized Ir-silicide phase was grown in ultrathin two-phase films on Si(001). Using transmission electron microscopy it was found to have the fluorite structure. Due to the misfit between this epitaxially stabilized phase and the silicon substrate, elastic and plastic strain relaxation can be observed. Optoelectronic measurements of transmission, resistivity, and Schottky barrier height show a transition from infrared absorbing to infrared transparent films depending on thickness and reaction temperature. First-principles calculations confirm the experimental data on the structure and electronic properties of fluorite-type Ir disilicide.

DOI: 10.1103/PhysRevB.79.104116 PACS number(s): 81.07.−b, 68.18.Jk, 68.37.Lp

I. INTRODUCTION

Hitherto, the research and particularly the technological development effort on epitaxial thin films were focused on materials which exhibit the same crystal geometry as a film and as a stable bulk crystal. Only few authors[1–3] investigated materials undergoing a strain-induced phase transformation when grown as thin epitaxial films on a suitable substrate. Such strain-induced phases are still usually considered as oddities. To understand their origin, deeper insight into the driving forces controlling epitaxial phase stabilization is necessary.

Previously published work consists predominantly of case studies. In contrast, von Känel's work on iron silicides is a rare example of an intentional search for an epitaxially stabilized phase: an orthorhombic bulk phase, here $FeSi_2$, transforms into a cubic phase when grown on Si(001).[1–3] In another work, von Känel described the transformation to an epitaxial monosilicide FeSi with a CsCl structure.[4] There have also been theoretical predictions for an epitaxially stabilized phase of CdTe.[5]

Presented here is a case study on an $IrSi_2$ phase which grows epitaxially on Si, and is strain stabilized and thus thickness limited. In the following we will give a brief overview over existing bulk stable Ir-silicide phases. The monosilicide IrSi crystallizes in the orthorhombic MnP structure which is related to the hexagonal NiAs structure and is metallic.[6] Amorphous IrSi (a-IrSi) is metallically bound as well.[7–9] It is assumed that in ultrathin films a two-dimensional electron gas forms. The phase Ir_3Si_5 was determined by Engström and co-workers.[10] The most noteworthy feature of the structural order is the alternating arrangement of filled and empty Si cubes which reflects structural elements reminiscent of the cubic fluorite structure. Ir_3Si_5 is the only known semiconducting Ir silicide. All the other phases are metallic. The polymorphic trisilicide $IrSi_3$ grows in an orthorhombic high-temperature phase and in a monoclinic low-temperature phase.[11–13]

Our paper is structured as follows. First in Sec. II we briefly describe the used experimental methods. This is followed by the results of transmission electron microscopy (TEM) diffraction measurements which are compared to high-resolution TEM (HRTEM) data in Sec. III. The confirmation of the resulting hypothesized model is provided by atomic resolution high-angle annular dark field (HAADF) imaging using aberration corrected dedicated scanning TEM (STEM). The TEM part of Sec. III ends with results on strain relaxation. Thereafter the results of the optoelectronic measurements yield the bonding state of the films and show that the films are thickness limited. Finally, the results of the first-principles calculations are presented which give the lattice parameter and the bonding state of $IrSi_2$. In the discussion, Sec. IV, we begin by excluding the possible formation of other silicides, then report the properties of the phase and relate the results to findings from literature.

II. EXPERIMENT

A. Sample growth

All samples were fabricated on *p*-Si(001) substrates with a nominal doping concentration of 7×10^{14} cm^{-3}. Layers for structural characterization were deposited onto bare Si wafers, while electro-optical measurements were performed on prefabricated planar IR-detector test structures on *n*-Si.[14] Test chips and plain wafers were processed simultaneously and under otherwise identical conditions in order to enable comparison between structural and electro-optical characterizations.

Prior to the Ir deposition, the substrates were cleaned in solvents (acetone, methanol) and rinsed in deionized water. The carbon contamination was removed by an oxidation step in hot Caro etch (one portion of 96% w/v H_2SO_4 and three portions of 30% w/v H_2O_2) and a further water rinse. The oxide was removed by diluted HF (1%), followed by a final water rinse in order to obtain a hydrogen-terminated surface. The samples were then blown dry in pure nitrogen and immediately loaded into a high-vacuum evaporation system where samples remain at room temperature (RT). Ir was

 ©2009 The American Physical Society

evaporated at a rate of 0.05–0.10 nm/s. The Ir film thickness was varied in steps between 0.3 nm and 8 nm, controlled by pietzo quartz and a mass spectrometer with an accuracy of 0.02 nm. A film inhomogeneity after deposition of less than 0.5% over a 4 inch wafer was determined by Rutherford backscattering diffraction.[14]

After the metal evaporation process the samples were loaded into a rapid thermal annealing (RTA) system with a base pressure of 1×10^{-5} mbar and annealed in nitrogen atmosphere at 700 °C for 300 s.

B. Transmission electron microscopy

TEM is the appropriate tool for investigation of ultrathin films because it allows structural and chemical information on atomic scale to be recorded simultaneously. A combination of different TEM techniques was used.

The samples were prepared with the standard preparation procedure using dimpling and subsequent Ar ion milling. Cross-section samples were prepared in ⟨100⟩ and ⟨110⟩ zone axes and plan-view samples in the [001] zone axis.

For HRTEM and some of the diffraction experiments a Philips CM 300 with a point resolution of 0.17 nm was used, operating at 300 kV acceleration voltage. Diffraction experiments on plan-view samples were performed in a Philips CM 30 operating at 300 kV.

In order to obtain diffraction intensities exclusively from the silicide film a Philips CM 300 with a field-emission gun was used operating at 300 kV with a probe diameter of approximately 3 nm.

All diffraction experiments were carried out in the selected area electron-diffraction (SAED) mode. The sample geometry made it necessary converging the beam slightly. As the intensities of the diffraction spots were only qualitatively evaluated, the change in shape caused by the beam convergence[15] could be tolerated. Kinematical simulations of the SAED patterns and thickness-defocus maps of the high-resolution contrast were calculated using the STADELMANN program package.[16]

In order to retrieve local chemical information on atomic scale HAADF measurements were performed at the Daresbury SuperSTEM laboratory. A VG STEM HB 501 equipped with a Nion Co. Mark II C_s corrector was used.[17] The microscope was operated at 100 keV with a 0.1 nm scanning probe, a 24 mrad probe convergence angle, and an angular acceptance range of the HAADF detector of (70–210) mrad. The HAADF signal increases monotonically with the atomic number of the scattering atoms, provided the sample thickness is suitable and not changing rapidly within the scanned area.[18] Thus C_s corrected HAADF imaging is a suitable method to investigate metal-silicon compounds with atomic resolution and, provided the right zone axis, to distinguish between pure metal and pure silicon atomic columns.[19,20] In the presented images, the variations in beam current caused by tip noise were removed by normalizing the average of each line of the image.

C. Optoelectronic measurements

1. IR absorption

The IR absorption a of the film was determined by measuring the IR transmittance t and reflectance r with the relation

$$a = 1 - t - r \tag{1}$$

while the absorption of the Si substrate was neglected. To determine the Schottky barrier the transmittance and reflectance were calculated dividing by a reference spectrum. The reference measurement for the transmittance was performed without the sample and for the reflectance, the reflectance of a gold mirror was used. The fixed reflection angle was 11° with respect to the surface normal.

An IR Fourier transform spectrometer (Bruker, type IFS 66 v/S) configured for MID-IR (~2–25 μm) and equipped with a globar, a KBr beam splitter, and a pyroelectric deuterated triglycin sulfate (DTGS) detector was used. The measurements were performed in the wavelength range from 1.8–5.9 μm with a resolution of 4 cm^{-1}. In order to eliminate interference with the ambient gas, the chamber was filled with dried and decarbonated air under a pressure of approximately 4 mbar.

2. Resistivity measurements

Resistivity measurements were carried out to study changes in the electronic properties of the different silicide films. For this the silicide films grown on the test structures (n-Si with a low doping concentration of approximately 7×10^{14} cm^{-3}) were used. Due to the high Schottky barrier height of Iridium silicide films on n-Si(001) the influence of the Si substrate on the resistivity measurements could be neglected. The resistivity was measured by the four-point method so that the influence of contact resistance was eliminated.

3. IR photoemission, IV measurements

Electro-optical measurements were used to deduce the bonding state in the films from the Schottky barrier height and the IR absorption. The evaluation of the experimentally determined infrared transmittance and reflectance gives the absorption and allows the bonding state of the film to be classified as either metallic or semiconducting or insulating. The stability range of the phases in the growth parameter window available from the experiments was determined.

The experiments were carried out with a black body radiator from the company CI systems, type SR2. The radiation arrives on the sample via passing narrow-band filters and two cryostate windows. The radiator is equipped with a set of 19 filters for wavelengths between 1.8 and 9.5 μm.

The transmittance of the band filters is >50% for the central wavelength and the band width is 2%–3.5% of the central wavelength. The temperature of the sample was adjusted between 35 K and RT with a helium evaporation cryostate and measured by a Pt100 resistor. We measured the photocurrent with a current-to-voltage converter and a lock-in amplifier in order to eliminate any derogation by the background radiation.

The incident power was calculated with Planck's formula and from the geometry of the experimental setting, the transmittance of the cryostate windows and the transmittance of the band filters. The photoresponsitivity R is then the ratio of the measured photo current I_{Ph} and the incident radiation

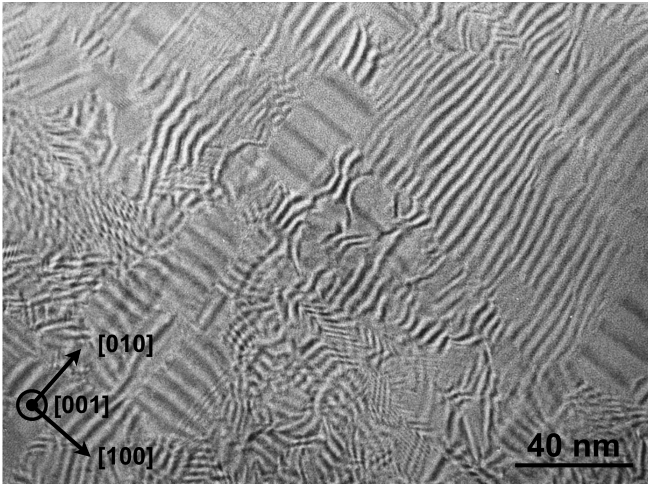

FIG. 1. Plan view in [001] zone axis of a Ir_xSi_y-$IrSi_2$ film grown from 2.0 nm deposited Ir at 700 °C.

power P_{in}. A suitable plot of $\sqrt{R}\cdot h\nu$ vs $h\nu$ (photon energy $E_{Ph}=h\nu$) allowed us to determine

$$R=\frac{I_{Ph}}{P_{in}}=C\left(\frac{h\nu-\Phi_B}{h\nu}\right)^2 \tag{2}$$

at different wavelengths, with the Fowler factor C and the Schottky barrier height $\Phi_{B,Ph}$. The Fowler factor C is a constant of the detector considering optical absorption and charge-carrier loss due to scattering.

III. RESULTS

A. TEM

After annealing to form the silicide layer three samples which had the initial Ir deposit thickness of 0.5 nm, 1.0 and 2.0 nm were prepared for electron microscopy. The silicide film thickness of these three samples of the series were determined from the high-resolution micrographs to be 1.25, 2.50, and 5.00 nm, varying by a step height of 2.7 nm or 0.54 nm, which is the height of one half or one unit cell of the silicon substrate parallel to the surface normal, respectively. The comparison of the initially deposited metal thickness to the resulting silicide layer shows an increase in the film thickness by a factor of 2.5 during annealing.

A typical plan view of the silicide film can be seen in Fig. 1. Careful analysis in cross section shows that the film consists of crystallite grains of two different phases, namely, $IrSi_2$ treated in this article and the domains of the crystallographically slightly different superstructure phase Ir_xSi_y, treated elswhere.[21] The moiré fringes which are visible in plan view are curved and vary significantly in distance. In such micrographs a distinction between the different phases and domains would be ambiguous.

However, the micrograph reveals initial information about the crystallite sizes and their distribution. The crystallites and domains are small and they appear to be inhomogeneous in size. The maximum crystallite size is about 200 nm in diameter, while most grains are much smaller. In case of resistivity and optical measurements we have to keep in mind, that we probe the average response of a thin film consisting of a patchwork of domains of two phases.

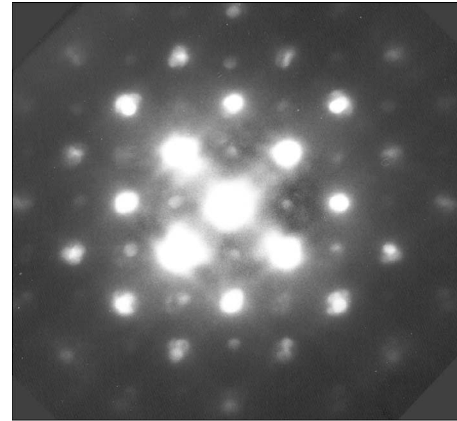

FIG. 2. Experimental diffraction pattern in [001] zone axis of the fluorite-type $IrSi_2$ with additional spots from silicon substrate.

A face-centered-cubic unit cell of $IrSi_2$ with a fluorite structure with a lattice constant of 0.565 nm ± 0.001 nm was determined from the experimental diffraction patterns in [001], [100], and [110] zone axes. Figures 2–6 show diffraction patterns with simultaneously collected intensities from the adjacent Si substrate in comparison with kinematical simulations of an $IrSi_2$ with a fluorite structure. In all zone axes experimental and simulated diffraction patterns correspond to each other in orientation and intensity distribution. Intensities from Si eclipse intensities from the silicide where diffraction conditions of both structures coincide. Diffraction spots of higher order allow the intensities of $IrSi_2$ and Si to be separated. Silicide diffraction spots fulfilling the diffraction conditions of the fluorite structure can be identified unequivocally due to the different lattice constants of silicide and silicon. The innermost 020-type spots appearing in the [001] and [100] zone axes diffraction patterns are forbidden for Si and cannot even arise from multiple scattering in Si. They can be caused by a fluorite structure though. There are some ambiguities concerning the formation of IrSi in zincblende structure which are clarified later in the discussion. The lattice misfit m between film and substrate $m=\frac{a_s-a_f}{a_f}$ is $m=3.8\%$.

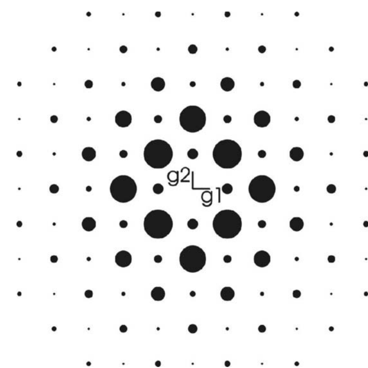

FIG. 3. Kinematical simulation of a diffraction pattern of fluorite-type $IrSi_2$ in [001] zone axis. Diffraction vectors are denoted as $g_1=[\bar{1}00]$ and $g_2=[010]$.

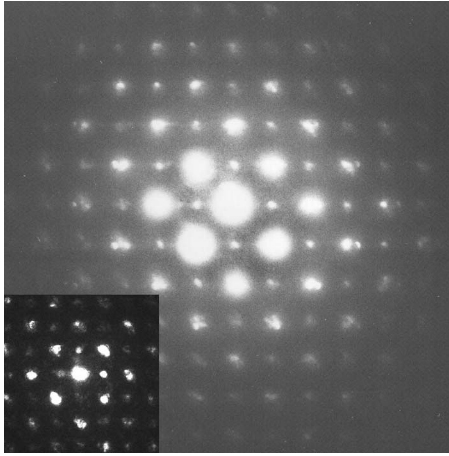

FIG. 4. Experimental diffraction pattern of the fluorite-type $IrSi_2$ in [100] zone axis from a sample prepared in cross section. The diffraction pattern shows additional spots from the silicon substrate. The inset shows diffraction spots from the film only. Both patterns correspond in arrangement and intensity distribution.

The high-resolution micrographs are in good agreement with the structure determination from electron-diffraction patterns. High-resolution contrast in [100] zone axis, see Fig. 7, together with the image simulations of $IrSi_2$ with a fluorite structure, see Fig. 8(c), are in correspondence, e.g., at 2.83 and 3.39 nm foil thickness. Moreover, electron-diffraction patterns and HRTEM micrographs show that the cubic phase grows epitaxially on the cubic Si(001) substrate.

The multislice simulations reproduce the relation between crystal structure and the high-resolution contrast for $IrSi_2$ having a fluorite structure [see Fig. 8(a)]. In [100] zone axis the interatomic distances in the cell projection, see Fig. 8(b), exceed slightly the resolution limit of 0.17 nm of the microscope. Thus a contrast was obtained that corresponds to column and interstitial positions of the crystal [see Fig. 8(c)]. The simulation was performed with a lattice constant of 0.565 nm $\pm$ 0.001 nm.

The final confirmation of fluorite structure was obtained from *Z*-contrast in atomic resolution HAADF images. Figure 9 taken in [100] zone axis and Fig. 10 in [110] zone axis show epitaxial growth of the films on the silicon substrate. In Fig. 9 it can clearly be seen that the Ir atoms form a lattice with fourfold symmetry, which correspond to a face-centered-cubic lattice in [100] projection epitaxially fixed on Si in the same projection. The interstices are not occupied by Ir. From the projection which is shown in Fig. 10 the distances of the high-resolution contrast maxima were evaluated to 0.4 nm. The aspect ratio r_a of the [001] axis and the ⟨110⟩ axis is $r_a = 1.4$, which corresponds to the expected value for a cubic unit cell. Thus the existence of a cubic $IrSi_2$ in the fluorite lattice with a lattice constant of 0.565 nm $\pm$ 0.001 is proven.

Lattice plane distances for the cubic CaF_2-type silicide and the strain have been estimated from the HAADF images [see Fig. 11]. The silicon substrate was used as reference. Measurements of lattice plane distances in the Fourier transform of image parts (see figure for real area size) show that the {100} and {110} plane distances (parallel to the interface) are the same for the silicon substrate and the epitaxial silicide film at coherent interface areas. The (001) distances perpendicular to the interface plane, however, differ considerably

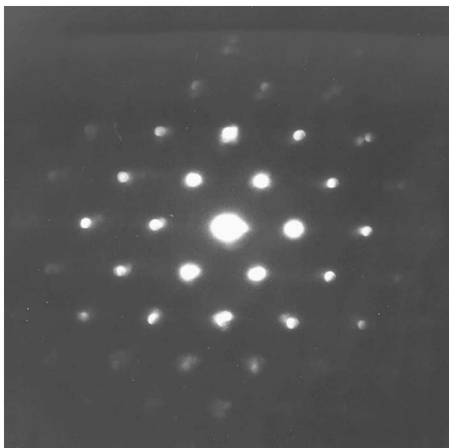

FIG. 5. Diffraction pattern in [110] zone axis of the fluorite-type $IrSi_2$ with additional spots from the silicon substrate.

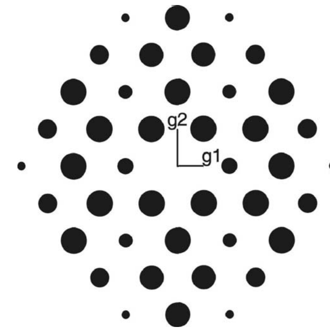

FIG. 6. Kinematical simulation of diffraction pattern in [110] zone axis. Diffraction vectors are denoted as $g_1 = [1\bar{1}0]$ and $g_2 = [001]$.

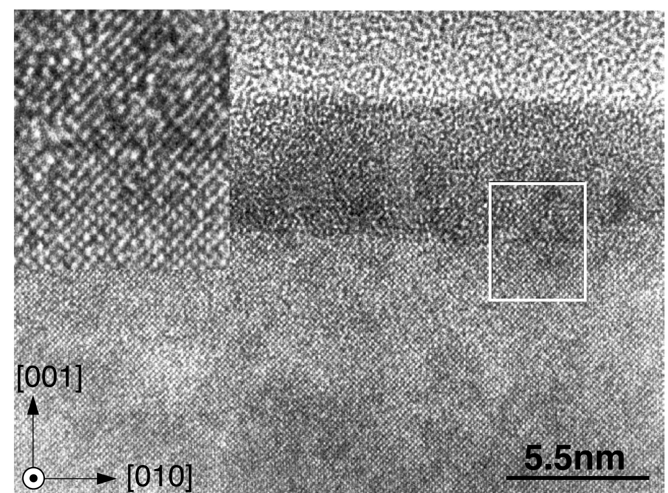

FIG. 7. Cross-section micrograph of $IrSi_2$ taken in [100] zone axis. The magnified view inset shows structure in accordance with simulations (see text for details), and also the perfect epitaxial relationship between film and Si substrate.

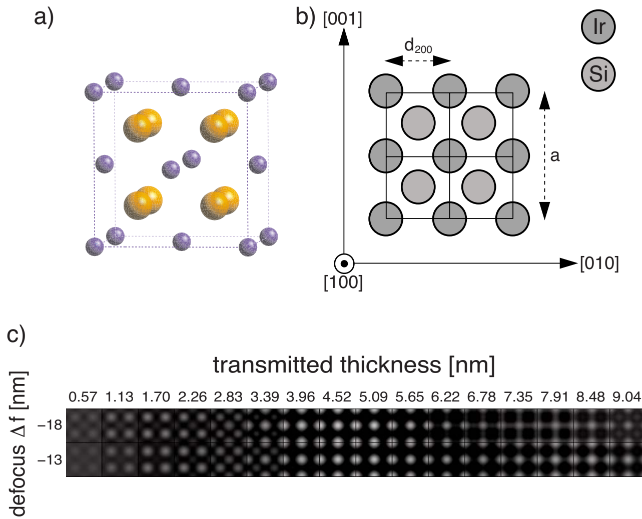

FIG. 8. (Color online) (a) Fluorite structure of $IrSi_2$. Ir atoms form the face-centered cell, Si atoms occupy the eight tetrahedral interstices. (b) Projection of the structure in [100] zone axis. (c) Calculated high-resolution contrast in [100] zone axis for a lattice constant of 0.565 nm. The contrast varies with thickness and defocus. Correspondence between lattice and image can be seen at particular thickness and defocus values, e.g., at 2.83 and 3.39 nm thickness.

(see comparison of Fourier transform of silicon and silicide in [001]) zone axis. In different film areas, where no crystal defects were apparent a local enlargement of the (001) silicide distance by a value of (8 to 18)% compared to the respective value of the silicon substrate was measured. That means, as expected for coherent epitaxial growth of a bigger crystal on a smaller, the silicide film is under compressive in-plane stress and expands parallel to the film normal. Nevertheless the degree of lattice distortion is high and might to some extent also be caused by the relaxation of the TEM sample which is thinned to a few nm thickness for electron transparency.

To derive the silicide lattice constant we assume a $d_{\mathrm{Si}(001)}$ of 0.543 nm for silicon close to the interface. We measured an expansion of the silicide in [001] direction of $13\pm5\%$. This leads to a lattice constant of 0.543 nm in [100] direction and a lattice constant of $0.614\ \mathrm{nm}\pm0.027\ \mathrm{nm}$ in [001] direction for the epitaxially stabilized iridium silicide film. Considering a really cubic stress-free bulk structure an average value between these two lattice constants of $d_{\mathrm{IrSi}_2\{100\}}=(0.578\pm0.027)$ nm can be estimated. The theoretically predicted lattice constant of 0.565 nm is well in the range of these experimental data.

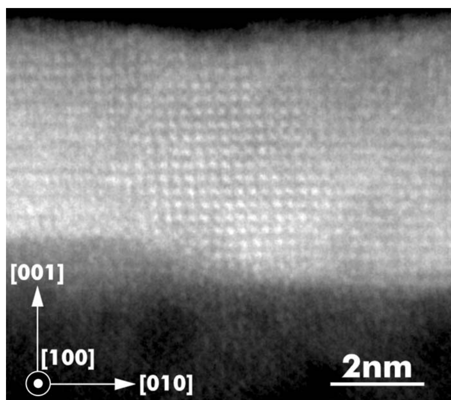

FIG. 9. HAADF micrograph of $IrSi_2$ in [100] zone axis.

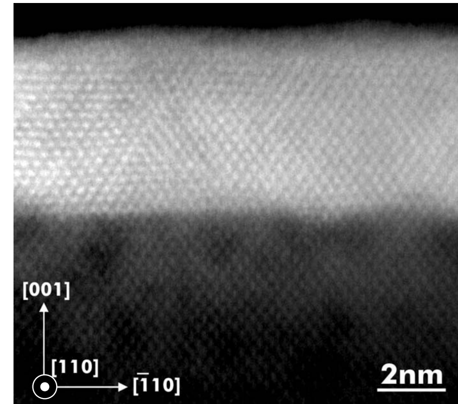

FIG. 10. HAADF micrograph of $IrSi_2$ taken in [110] zone axis.

Careful inspection of the data reveals the cubic silicon lattice as derived from the scanned dark field image to be deviated by 0.7 degrees from the supposedly cubic symmetry, i.e., 90 degrees. This is caused by a slight difference in magnification in the two scanning directions. De-skewing the images prior to the geometric measurements would be possible but would not add information to the results extracted directly from the raw data since the deviation is small (0.8%) compared to the measured lattice expansion range and because silicon from the same image was used as a reference.

Elastic and plastic strain relaxation were observed in the silicide films and could be attributed to the high misfit of $m=3.8\%$. The fluorite phase shows surface undulations, i.e., rippling which occurs independent of the interface curvature or roughness (Fig. 12). Surface undulations allow the crystal lattice to relax the stored strain elastically via the surface. This is described by the theory of epitaxial growth, e.g., by Stranski-Krastanov growth.[22] With respect to cooperating mechanisms in strain relaxation surface undulations are in particular treated by Albrecht.[23]

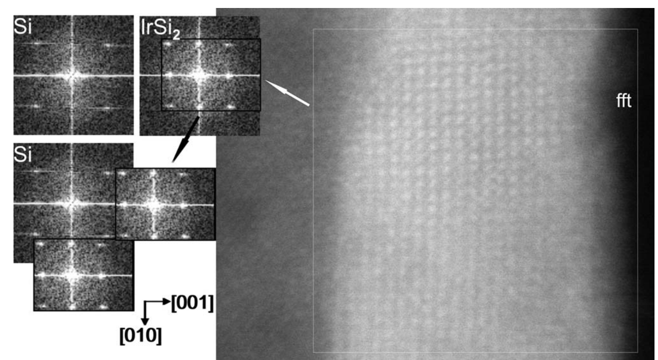

FIG. 11. Elastic strain in $IrSi_2$ on Si(001). Dark field STEM image of $IrSi_2$. Insets show Fourier transforms of film and substrate from which the strain was determined.

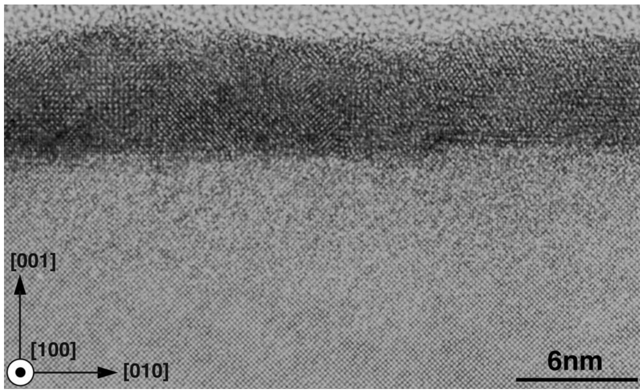

FIG. 12. Cross-section micrograph of surface undulations of the film grown from 2.0 nm Ir deposit at 700 °C ($IrSi_2$ taken in [100] zone axis).

Plastic relaxation features of the silicide films are shown in Fig. 13. For a deeper understanding of the plastic relaxation phenomena the slip direction ⟨112⟩ or ⟨110⟩ and the shear value have to be determined. The clarification of these planar defects could answer a further question, namely, whether relaxation mechanisms can lead to the formation of the equilibrium structure of Ir_3Si_5.

B. Optoelectronic measurements

1. IR absorption

In Fig. 14 the infrared-optical absorption of the annealed silicide films at $\lambda=4$ μm is plotted versus the thickness of the initially deposited iridium layers. The absorption curve increases with the initial metal layer thickness up to a critical value of 2.6 nm Ir. Beyond this critical value absorption breaks down. High IR absorption is indicative of a metallic bonding state in the silicide film formed up to 2.6 nm of nominally deposited Ir. Beyond this thickness the break down in IR absorption indicates the formation of the semiconducting Ir_3Si_5 phase. The semiconducting Ir_3Si_5 is widely reported to be the equilibrium phase at 700 °C.[10,12,13,25]

2. Resistivity

The resistivity of the thinnest silicides (of 1.25 nm) was compared to the crystalline monosilicide (c-IrSi) of 13.5 nm

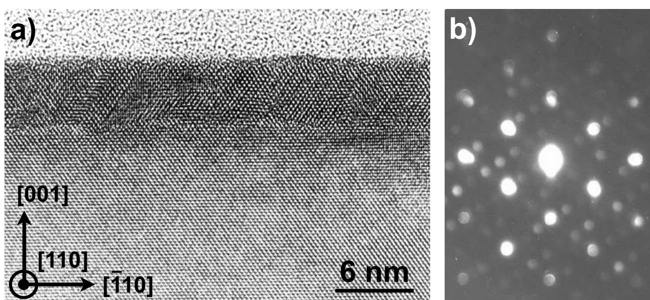

FIG. 13. Periodic faults in $IrSi_2$ in [110] zone axis. (a) Cross-section micrograph showing faults generated by adjacent *A*- and *B*-type cubic $IrSi_2$, which appear periodically in the film. (b) The respective experimental diffraction pattern of the silicide film showing the extra spots typical for *A*- and *B*-type in front of each other in the electron beam (Ref. 24).

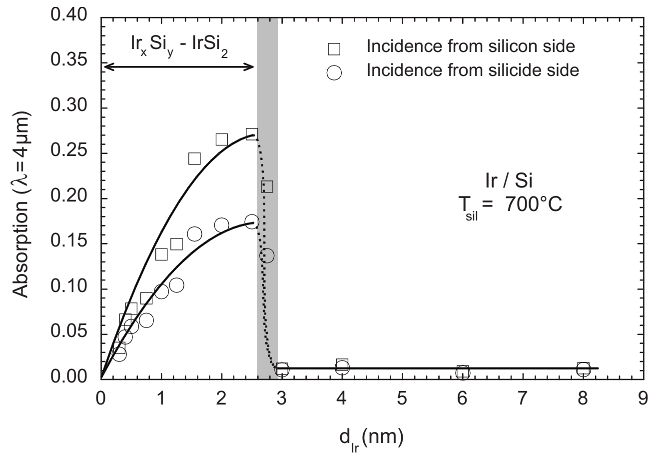

FIG. 14. Optical absorption of Ir silicide/Si(001) at $\lambda=4$ μm vs the deposited Ir thickness for illumination from silicon and silicide side. The gray bar marks the critical thickness to which the high absorption is limited. The lines should guide the eye.

thickness grown at 500 °C [see Fig. 15]. The resistivity of c-IrSi measures $\rho=400$ $\mu\Omega$ cm and c-IrSi is thus considered to be a metal.[7] The thin-film patchwork of the Ir silicides, $IrSi_2$ and Ir_xSi_y, reveals a resistivity of about $\rho \simeq 900$ $\mu\Omega$ cm. This value is constant for the investigated temperature range. The electrical conductivity $\sigma_{el}=1.5 \times 10^3$ Ω^{-1} cm^{-1}, thus the film can be considered as metallic.

3. IR photoemission and IV measurements

The Schottky barrier height was determined at 50 K by two independent methods, photoemission and *I-V* curves. Figure 16 shows the Schottky barrier height plotted vs the annealing temperature for films grown from 0.5 nm Ir. Between 550 and 650 °C the values decrease continuously. Beyond 650 °C the decay is flatter and ends at 730 °C with 130 meV for the Schottky barrier height from photoemission measurements and 85 meV for the Schottky barrier height evaluated from *I-V* curves. While the shapes of both curves agree rather well, the quantitative difference is still a matter

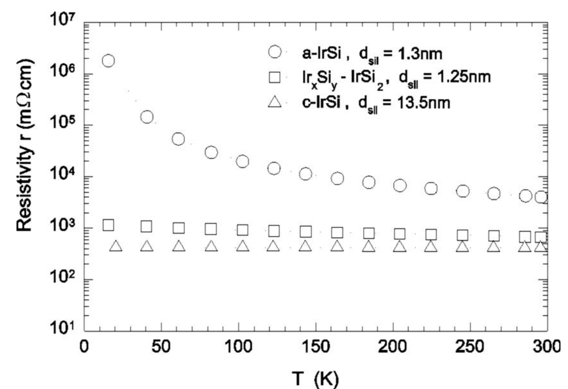

FIG. 15. Resistivity vs temperature (K). The phases a-IrSi and c-IrSi grow at 500 °C annealing temperature dependent on the thickness of the initially deposited iridium layer. In thicker films c-IrSi grows. The phases Ir_xSi_y and $IrSi_2$ grow at 700 °C annealing temperature.

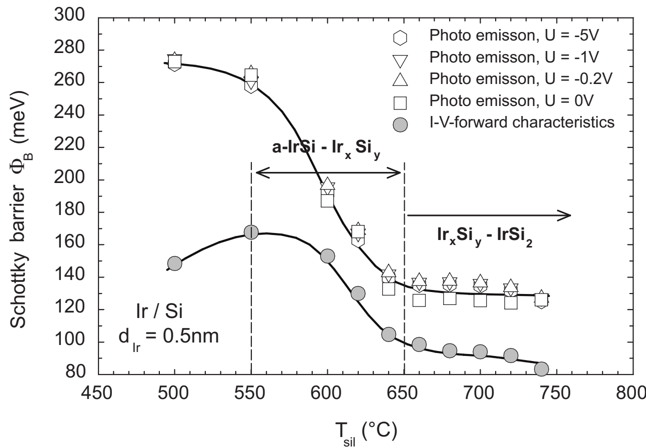

FIG. 16. Schottky barrier Φ_B vs annealing temperature determined from photoemission and *I-V* curves. The thickness of the initially deposited iridium layer is $d_{\mathrm{Ir}}=0.5$ nm.

of discussion and not yet clarified.[26] Nevertheless, the results of both methods reveal a metallic bonding state in the investigated films.

C. First-principles calculations

To confirm our suggestion that $IrSi_2$ can be epitaxially stabilized in a fluorite phase we performed first-principles density-functional-theory calculations for this structure as well as two other alternative structures. The microscopy data show unambiguously that $IrSi_2$ possesses cubic symmetry with an fcc Bravais lattice. The fluorite structure, see Fig. 8, is the most probable candidate. However, in principle, an alternative cubic structure with fcc periodicity and the same atomic density is possible. This structure can be referred to as "dense" zincblende-type structure, see Fig. 17, with the second Si atom sitting at the cube center. It has the same number of atoms in the elementary cell as the fluorite structure. The Ir atom together with the Si atom at the cube center generates a NaCl-type sublattice while the remaining Si atoms occupy half of the tetrahedral sites. Since this structure and the fluorite structure both have the same number of atoms it is straightforward to rule out one of them by comparing their total energies. We have also performed calculations for a hypothetical IrSi crystal in a standard zincblende structure. Although this structure has a different stoichiometry than the fluorite $IrSi_2$ structure, it also possesses cubic symmetry with fcc translational periodicity and, in principle, may be an alternative candidate for an epitaxially stabilized cubic IrSi phase. To exclude this structure we calculated its lattice constant to compare it with the experimental value. In addition, we have calculated the bulk moduli for these structures as well as the electronic density of states (DOS) for the fluorite structure.

The calculations were performed with a full-potential linear muffin-tin orbital (FPLMTO) method[27,28] that makes no shape approximation for the crystal potential. The crystal is divided into regions inside atomic spheres and an interstitial region. Inside the atomic spheres the scalar-relativistic radial Schrödinger equation is solved numerically. This solution is matched to a Hankel function at the sphere boundary, thus providing the LMTO basis functions. Spin-orbit interactions were neglected.

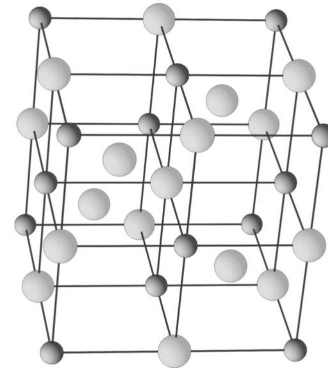

FIG. 17. Illustration of the "dense" zincblende-type structure. As in Fig. 8 the origin is chosen so that the Ir atoms are located at the corners. In contrast to the rocksalt structure half of the interstitial sites are occupied with Si atoms.

Figure 18 shows the total energies versus lattice constant for the two cubic $IrSi_2$ structures. The solid curves are obtained by fitting the calculations to Murnaghan equations of state.[29] The fluorite structure is indeed energetically much more favorable than the dense zincblende structure. The bulk moduli for the two structures are $B_0=2.00$ Mbar (fluorite) and $B_0=1.86$ Mbar ("dense" zincblende). The calculated lattice parameter for the fluorite-type $IrSi_2$ structure is $a=5.65$ Å, which agrees very well with the experimentally determined lattice constant. This result supports our hypothesis that the cubic fluorite $IrSi_2$ structure is epitaxially stabilized on Si(001).

For a "standard" zincblende IrSi structure the calculations predict a lattice constant of 5.27 Å, which is substantially smaller than the lattice parameter of Si(5.43 Å) and the lattice constant measured by TEM.

In Fig. 19 the density of electronic states for fluorite $IrSi_2$ is plotted (in electrons per eV per unit cell). The Fermi level

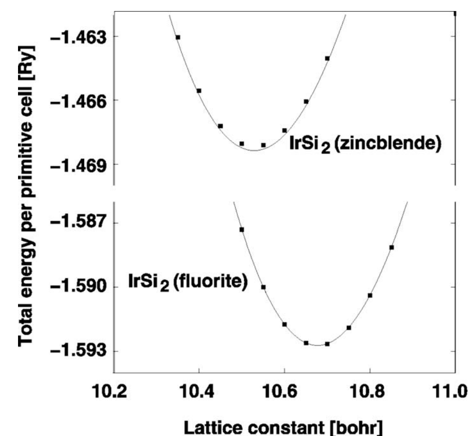

FIG. 18. Total energy per primitive cell as a function of lattice constant for $IrSi_2$ in the fluorite structure and a "dense" zincblende structure. The total energy of the fluorite structure is lower than that of the dense zincblende structure.

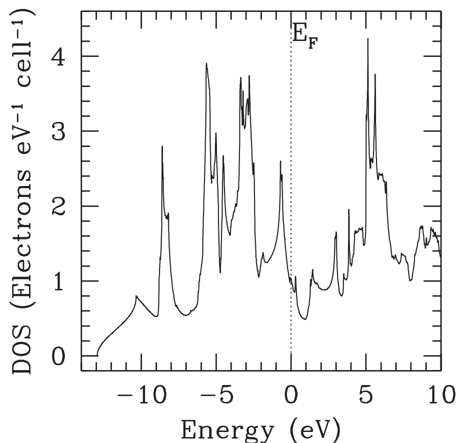

FIG. 19. Electronic density of states (DOS) versus energy for $IrSi_2$ in the fluorite structure. The Fermi energy E_F is taken at the zero of energy.

E_F is located slightly above the DOS peaks arising from Ir d states. Fluorite $IrSi_2$ is thus clearly metallic. In fact, E_F is quite close to a local DOS minimum. However the DOS does nowhere reach zero. Between −3 and −5.5 eV the DOS peaks correspond to the Ir-Ir d bonds and to the Ir(d)-Si(p) bonds. These bonds are much stronger than the Si(s)-Si(s) bonds at −8.5 and −10 eV.

IV. DISCUSSION

First in this chapter, further evidence for the formation of the proposed fluoride silicide structure instead of a zincblende IrSi will be provided, supporting the results from the first-principles calculations. Then the properties and growth behavior of the investigated silicide films will be discussed.

The reaction temperature of 700 °C used here lies far above the formation temperature and stability field of known Ir-monosilicide phases. According to the reaction kinetics of Ir silicides, monosilicides are formed between 400 and 600 °C. Between 500 and 700 °C the bulk stable Ir_3Si_5 forms. Thus, with 700 °C deposition temperature the used regime was beyond monosilicide formation.[26,30–32]

The film thickness increased during annealing by a factor of 2.5. Taking into account the experimentally determined lattice constant of 0.565 nm ± 0.001 nm the conclusion can be drawn that the chemical ratio of Ir:Si is larger than 1:1, namely 1:2. An IrSi in the structurally related cubic zincblende structure would have consumed less Si for its formation. Thus, also considering structural data as well as the growth parameters the formation of a IrSi in zincblende structure can be excluded.

As to the properties and growth of the investigated thin films, the results of the electrical, optoelectronic, and optical measurements reveal that the films which, as mentioned in Sec. I, contain two Ir-silicide phases are metallic up to a critical silicide film thickness H_c of 6 nm and a critical initial metal layer thickness of 2.6 nm, respectively. Beyond this critical thickness the films are transparent to IR radiation, which indicates a change in the bonding state to a semiconducting phase. The only known semiconducting silicide is the bulk stable Ir_3Si_5. From that it can be concluded that in thicker films Ir_3Si_5 forms.

The measurements show that the existence of the phases is thickness limited. This finding will be inspected now in more detail. Two different crystal phases with different bonding states grown under otherwise identical growth conditions were observed. Below the critical thickness H_c $IrSi_2$ and a Ir_xSi_y superstructure[21] were found, and above this critical thickness only the bulk stable Ir_3Si_5. The bulk stable phase can be related to the epitaxially stabilized fluoride phase via a structural phase transformation due to structural similarities as mentioned in Sec. I. An analogous case was observed by Mäder and von Känel for $FeSi_2$, which can be grown as a metal in the fluorite structure on Si(001) or as a semiconductor in the bulk stable tetragonal lattice.[33] In contrast to the $FeSi_2$ case, in case of Ir silicide the phase transformation is accompanied by a slight change in stoichiometry. For reasons which are explained by Hörmann[21] this change can be attributed to a kinetic effect.

The $IrSi_2$ phase grows semicoherently on Si(001). The fluorite-type $IrSi_2$ has a lattice mismatch $f=3.8\%$ to the Si substrate, and as a consequence the films contain many different defects. The TEM micrographs show that the $IrSi_2$ phase contains defects, such as dislocations and stacking faults as a consequence of plastic relaxation of the lattice misfit to the substrate. Surface undulations are considered to be a result of elastic strain relaxation.[23] The formation of these defects is well understood.[34] Up to a critical thickness a misfitting epitaxial film grows defect free. Beyond this critical thickness misfit dislocations or surface undulations occur, providing plastic and elastic strain relaxation, respectively. Nevertheless and despite the defects, residual strain can remain in ultrathin epitaxially stabilized films if their lattice mismatch to the substrate is sufficiently high. Due to the finite size of the crystals parallel to the growth direction, this residual strain is always nonhydrostatic plain strain, independent of whether partial strain relaxation occurred or not. Thus it can be concluded that the nonhydrostatic plain strain state plays a crucial role in the formation and stability of the silicide phases within a limited thickness range.

V. CONCLUSION

A metallic $IrSi_2$ with a fluorite structure has been described which is exclusively stable in ultrathin films up to 6 nm thickness. In thicker films the semiconducting Ir_3Si_5 grows. The origin and stability of the phase is interpreted by semicoherent growth on the silicon substrate and by nonhydrostatic plain strain. The phase can be related to the bulk stable phase via a structural phase transformation.

Similar phase stabilization mechanisms can be predicted for other film-substrate couples. Promising candidates fulfill the following prerequisites formulated by Zunger.[35] The bulk stable film material must have a large bulk modulus, which means it must be sufficiently stiff. The crystal lattice of the bulk stable phase must have a structural relationship to the substrate, i.e., both need to have similar atomic arrangements or similar structural elements, to allow for a structural trans-

formation under strain. Furthermore, the bulk stable phase and the strain-stabilized phase must have a similar enthalpy of formation.

We predict a transformation as in the case described above for $OsSi_2$ on Si(001). Os has the lowest experimentally determined compressibility; it is reported to be stiffer than diamond.[36] Thus it is expected that the bulk stable orthorhombic $OsSi_2$ is fulfilling Zungers criterion of a large bulk modulus. Furthermore, the crystal structure of $OsSi_2$ is built up of alternating sequences of filled and empty Si cubes as it is the case for Ir_3Si_5 and the fluorite-type lattices[37] reported here. Therefore, suitably strained ultrathin films of $OsSi_2$ are expected to grow in the fluorite structure.

ACKNOWLEDGMENTS

Part of this work was carried out at the Central Facility for High Resolution Electron Microscopy of the Friedrich-Alexander University Erlangen-Nürnberg. U.H. wants to thank the Institute of Inorganic Materials Chemistry of the University of Bonn and the Max-Planck Institute of Microstructural Physics in Halle for the excellent technical support at their microscopes. A.B. and M.F. thank the EPSRC for funding the SuperSTEM facility. The work of J.E.K. was performed under the auspices of the U.S. DOE by the University of California Lawrence Livermore National Laboratory under Contract No. W–7405–Eng–48.

*Present address: Universität Ulm, Materialwissenschaftliche Elektronenmikroskopie, Albert-Einstein-Allee 11, 89069 Ulm, Germany.

†Present address: Leibniz-Institut für Kristallzüchtung, Max-Born-Strasse 2, 12489 Berlin, Germany.

‡Present address: Bruker-AXS Microanalysis GmbH, Schwarzschildstrasse 12, 12489 Berlin, Germany.

[1] H. von Känel, R. Stalder, H. Stirringhaus, N. Onda, and J. Henz, Appl. Surf. Sci. **53**, 169 (1991).

[2] K. A. Mader, H. von Kanel, and A. Baldereschi, Phys. Rev. B **48**, 4364 (1993).

[3] H. von Känel, C. Schwarz, S. Goncalves-Conto, E. Müller, L. Miglio, F. Tavazza, and G. Malegori, Phys. Rev. Lett. **74**, 1163 (1995).

[4] H. von Känel, M. Mendik, K. A. Mäder, N. Onda, S. Goncalves-Conto, C. Schwarz, G. Malegori, L. Miglio, and F. Marabelli, Phys. Rev. B **50**, 3570 (1994).

[5] S. Froyen, S. H. Wei, and A. Zunger, Phys. Rev. B **38**, 10124 (1988).

[6] W. L. Korst, L. N. Finnie, and A. W. Searcy, J. Phys. Chem. **61**, 1541 (1957).

[7] D. Wörle, H. Grünleitner, K. M. Mahlein, and M. Schulz, Phys. Status Solidi A **167**, 107 (1998).

[8] D. Wörle, H. Grünleitner, V. Demuth, C. Kumpf, H. P. Strunk, E. Burkel, and M. Schulz, Appl. Phys. A: Mater. Sci. Process. **A66**, 629 (1998).

[9] H. Grünleitner, K. Semmelroth, and M. Schulz. Phys. Status Solidi A **185**, 429 2001.

[10] I. Engström, Th. Lindsten, and E. Zdansky, Acta Chem. Scand., Ser. A **41a**, 237 (1987).

[11] I. Engström and E. Zdansky, Acta Chem. Scand., Ser. A **36a**, 857 (1982).

[12] M. Wittmer, P. Oelhafen, and K. N. Tu, Phys. Rev. B **33**, 5391 (1986).

[13] C. E. Allevato and C. B. Vining, J. Alloys Compd. **200**, 99 (1993).

[14] H. Mahlein, Ph.D. thesis, Friedrich-Alexander-Universität Erlangen-Nürnberg, 1999.

[15] D. B. Williams and C. B. Carter, *Transmission Electron Microscopy. A Textbook for Materials Science* (Plenum, New York, 1996), Vol. I.

[16] P. A. Stadelmann, Ultramicroscopy **21**, 131 (1987).

[17] O. L. Krivanek, N. Dellby, and A. R. Lupini, Ultramicroscopy **78**, 1 (1999).

[18] S. J. Pennycook and D. E. Jesson, Phys. Rev. Lett. **64**, 938 (1990).

[19] U. Falke, A. Bleloch, M. Falke, and S. Teichert, Phys. Rev. Lett. **92**, 116103 (2004).

[20] M. Falke, U. Falke, A. Bleloch, S. Teichert, G. Beddies, and H.-J. Hinneberg, Appl. Phys. Lett. **86**, 203103 (2005).

[21] U. Hörmann, Ph.D. thesis, Friedrich-Alexander-Universität Erlangen-Nürnberg, 2004.

[22] I. N. Stranski and L. von Krastanow, Sitzungsber. Akad. Wiss. Wien, Math.-Naturwiss. Kl., Abt. 2B **146**, 797 (1939).

[23] M. Albrecht, S. Christiansen, J. Michler, W. Dorsch, H. P. Strunk, P. O. Hansson, and E. Bauser, Appl. Phys. Lett. **67**, 1232 (1995).

[24] S. Teichert, M. Falke, H. Giesler, G. Beddies, and H.-J. Hinneberg, Thin Solid Films **336**, 222 (1998).

[25] S. Petersson, J. A. Reimer, M. H. Brodsky, D. R. Campbell, F. d'Heurle, B. Karlsson, and P. A. Tove, J. Appl. Phys. **53**, 3342 (1982).

[26] H. Grünleitner, Ph.D. thesis, Friedrich-Alexander-Universität Erlangen-Nürnberg, 2001.

[27] M. Methfessel, Phys. Rev. B **38**, 1537 (1988).

[28] M. Methfessel, C. O. Rodriguez, and O. K. Andersen, Phys. Rev. B **40**, 2009 (1989).

[29] F. D. Murnaghan, Proc. Natl. Acad. Sci. U.S.A. **30**, 244 (1944).

[30] S. Petersson, J. Baglin, W. Hammer, F. d'Heurle, T. S. Kuan, I. Ohdomari, J. de Sousa Pires, and P. Tove, J. Appl. Phys. **50**, 3357 (1979).

[31] I. Ohdomari, T. S. Kuan, and K. N. Tu, J. Appl. Phys. **50**, 7020 (1979).

[32] I. Engström and F. Zackrisson, Acta Chem. Scand. (1947-1973) **24**, 2109 (1970).

[33] K. A. Mäder, H. von Känel, and A. Baldereschi, Phys. Rev. B **48**, 4364 (1993).

[34] D. J. Srolovitz, Acta Metall. **37**, 621 (1989).

[35] A. Zunger, *Handbook of Crystal Growth* (Elsevier Science, Amsterdam, 1994), Vol. 3b, Chap. 22, p. 997.

[36] H. Cynn, J. E. Klepeis, C.-S. Yoo, and D. A. Young, Phys. Rev. Lett. **88**, 135701 (2002).

[37] I. Engström, Acta Chem. Scand. (1947-1973) **24**, 2117 (1970).